Galileo Multispectral Imaging of the North Polar and Eastern Limb Regions of the Moon

M. J. S. Belton,* R. Greeley, R. Greenberg, A. McEwen, K. P. Klaasen, J. W. Head III, C. Pieters, G. Neukum, C. R. Chapman, P. Geissler, C. Heffernan, H. Breneman, C. Anger, M. H. Carr, M. E. Davies, F. P. Fanale, P. J. Gierasch, A. P. Ingersoll, T. V. Johnson, C. B. Pilcher, W. R. Thompson, J. Veverka, C. Sagan

Multispectral images obtained during the Galileo probe's second encounter with the moon reveal the compositional nature of the north polar regions and the northeastern limb. Mare deposits in these regions are found to be primarily low to medium titanium lavas and, as on the western limb, show only slight spectral heterogeneity. The northern light plains are found to have the spectral characteristics of highlands materials, show little evidence for the presence of cryptomaria, and were most likely emplaced by impact processes regardless of their age.

Imaging objectives at Galileo's second lunar encounter with the moon (EM-2) were to extend multispectral mapping of the western limb and far side (*1–5*) to the northeastern limb and north polar regions. During the lunar flyby, seven multispectral mosaics (LUNMOS 1 to 7) were constructed (Figs. 1 and 2) on regions not previously observed with a modern digital camera. These data also provide a quantitative cross-calibration with regions for which spectral data already exist including MS2 [a spectrophotometric standard area in Mare Serenitatis (*6, 7*)], Apollo and Luna landing sites, and parts of the near side observed from Galileo during EM-1. The solid-state imaging (SSI) filter set and its applications to the moon are described in (*8*). The best spatial resolution of 1.1 km per pixel was obtained for LUNMOS 4 centered over the eastern Mare Frigoris region. This resolution is an improvement of about three times over that achieved at EM-1.

The Humboldtianum basin (61°N, 84°E) (Fig. 1, C and D) is a possible double- or triple-impact basin and is Nectarian in age (*9, 10*). Data from the EM-2 encounter clearly show the distinctive polygonal shape of the outer (second) ring in the southeast quadrant of the basin (*11*). In addition, the illumination geometry highlights the radial texture of the deposits in the southeastern sector, between the second and first ring, that indicate that the inner ring (275 km in diameter) is equivalent to the rim crest of the excavation cavity (*10*). Galileo stereoscopic images show that the outer ring corresponds to the main topographic rim of the basin. The spectral characteristics of Humboldtianum deposits are similar to those typical of highlands and indicate crustal homogeneity through the excavation depth of the impact. A few patches in the Imbrian age light plains (*9*) within the basin show possible mafic signatures but they are small and further spectral analysis is required for verification as mare deposits.

Images from the EM-2 encounter cover the northern rim and ejecta deposits of the Imbrium basin (33°N, 18°W) (Fig. 1A), including areas with "Imbrium sculpture" (*10*). The Alpes and Fra Mauro formations have spectral characteristics similar to those of mature highland soils. Two craters superposed on the ring (Plato, 101 km in diameter; Iridum, 260 km in diameter) display anomalously red rims (Fig. 1, A, B, E, and F). The red signature of Plato can be traced well into the continuous ejecta deposits (*12*). Impact melt may contribute to this signature (see below), or the deposits may represent material excavated from great depths (*2, 3*).

Light plains, typified by the Cayley formation investigated during Apollo 16 (*13*), are smooth, level units morphologically similar to maria but with albedos comparable to those of highlands. Their origin, volcanic or from impact, has been controversial (*14*). Mainly Imbrian age and older than most mare units (*4, 15*), their largest concentration is in the previously poorly imaged sector between Mare Frigoris and the lunar north pole (Fig. 1, A and B) (*9, 13*), well covered by Galileo. Although many light plains deposits in this region are mantled with ejecta from young craters such as Anaxagoras (Fig. 1, A and B), Galileo data indicate that the older (early Imbrian) (*9*) light plains have spectra typical of highlands. In the case of the younger regions, which may involve mare materials marked by thin, high-albedo deposits (*16*) such as cryptomaria (*17*), the Galileo data (Fig. 3) show that they also have highlands spectral signatures, that is, the plains near craters Gärtner and Thales are spectrally similar to Apollo 16 highlands (Fig. 3C). Nevertheless, a few small, fresh craters do have mafic spectral signatures that might indicate cryptomaria (*18*) (Fig. 3B); for example, the dark-halo crater, Gärtner D, has spectral affinities with mare basalt (*19*). This crater is about 100 km from the nearest exposed basalts that are found in Mare Frigoris, although its ejecta deposits (Fig. 3B) are similar to the medium high titanium basalts of Mare Imbrium. This is the strongest evidence for the presence of mare deposits beneath the northern light plains, and although there are many reasons why cryptomaria may escape identification (*20*), the new data show that cryptomaria are not widespread in northern latitudes as in the Schiller-Schickard area (*1–5, 16, 18, 21*) and that the northern light plains appear to have been emplaced through impact processes.

Mare deposits are commonly characterized by their titanium content, which provides insight into their magma sources and the petrologic history of the lavas erupted onto the surface. A measure of the TiO_2 content of mature mare soils was derived from 413/560-nm ratio images, with the use of a classification scheme in which "low" titanium is <2% TiO_2, "medium" titanium is <4% TiO_2, "medium-high" titanium is 3 to 7% TiO_2, and "high" titanium is >6% TiO_2. Overlapping values in this scheme result from uncertainties in the empirical relation between spectral signature and titanium content derived from Charette and colleagues (*22*). The results were compared with ages derived from crater statistics to assess trends in lunar volcanism in the areas observed for comparison with the near side. The techniques used and the uncertainties in the age estimates are addressed in (*4, 15*).

M. J. S. Belton, National Optical Astronomy Observatories, Tucson, AZ 85719, USA.
R. Greeley, Department of Geology, Arizona State University, Tempe, AZ 85287–1404, USA.
R. Greenberg and P. Geissler, Lunar and Planetary Laboratory, University of Arizona, Tucson, AZ 87721, USA.
A. McEwen, U.S. Geological Survey, Flagstaff, AZ 86001, USA.
K. P. Klaasen, C. Heffernan, H. Breneman, T. V. Johnson, Jet Propulsion Laboratory, California Institute of Technology, Pasadena, CA 91109, USA.
J. W. Head III and C. Pieters, Department of Geology, Brown University, Providence, RI 02912, USA.
G. Neukum, Deutsche Forschungsanstalt fur Luft und Raumfahrt, 8031 Oberpfaffenhofen, Federal Republic of Germany.
C. R. Chapman, Planetary Science Institute, Tucson, AZ 85719, USA.
C. Anger, Institute for Space and Terrestrial Science, Concord, Ontario, Canada L4K 3C8.
M. H. Carr, U.S. Geological Survey, Menlo Park, CA 94025, USA.
M. E. Davies, RAND, Santa Monica, CA 90406, USA.
F. P. Fanale, Institute of Geophysics, University of Hawaii, Honolulu, HI 96822, USA.
P. J. Gierasch, W. R. Thompson, J. Veverka, C. Sagan, Department of Astronomy, Cornell University, Ithaca, NY 14853, USA.
A. P. Ingersoll, California Institute of Technology, Pasadena, CA 91125, USA.
C. B. Pilcher, NASA Headquarters, Washington, DC 20546, USA.

*To whom correspondence should be addressed.

Mare Humboldtianum is within the inner ring of the Humboldtianum basin (Fig. 1, C and D). Differences in albedo and the densities of superposed impact craters suggest that more than one mare unit is present. Its western margin has a low 413/560-nm ratio, indicative of low-titanium basalt soils, and a cratering model age of 3.57×10^9 years ago (3.57 Ga). Similar lavas also fill an unnamed 35-km, mare-flooded crater adjacent to the western lavas marked F in Fig. 1D. Most of Mare Humboldtianum is slightly younger (3.48 Ga) and has a higher 413/560-nm ratio, indicating medium-titanium basalt soils. Parts of eastern Mare Humboldtianum have slightly higher 756/986-nm ratios, but this difference is attributed to contamination by ejecta from the Copernican age craters Hayn and Bel'kovich K. Mare deposits also occur as small, isolated patches on the western side of the Humboldtianum basin between the first and second ring. These deposits appear to be low to medium titanium basalts. Other isolated mare deposits occur in many locations west and south of the Humboldtianum basin. The SSI data indicate that mare soils on the floor of crater Endymion (Fig. 1C) are derived from medium titanium lavas and that mare patches south and east of Endymion are low to medium titanium basalt soils, consistent with Mariner 10 data (*23*). The Endymion mare has a cratering model age of 3.63 Ga; Lacus Temporis (a mare deposit south of Endymion) ranges in age from 3.65 to 3.73 Ga. In contrast, Lacus Spei, a low albedo, lightly cratered mare patch south of crater Mercurius, has a cratering model age of 3.55 Ga and appears to be a medium titanium basalt, also consistent with Mariner 10 results.

The Crisium basin (*24*) contains a variety of mare deposits (*7*, *25*), and samples with very low (<1 weight % TiO_2) Ti content were returned to Earth by Luna 24 (*26*). The EM-2 data, however, indicate that many of the Mare Crisium soils are derived from predominantly medium and medium high titanium lavas, a result consistent with Earth-based observations. Areas not characterized previously include Mare Anguis, the northeast margin of Mare Crisium, and the floor of crater Cleomedes. Materials in these areas have 413/560-nm ratios indicative of medium-titanium basalt soils. Mare deposits in Mare Undarum and Mare Spumans were found to be medium titanium basalt soils.

The diversity of mare basalt soils in northern Mare Frigoris is exemplified by the spectra for M. Frigoris and Blue mare in Fig. 3B. The former is interpreted to be a low titanium basalt soil, perhaps iron-rich; the latter is a medium to medium high titanium basalt soil that bears spectral affinities with

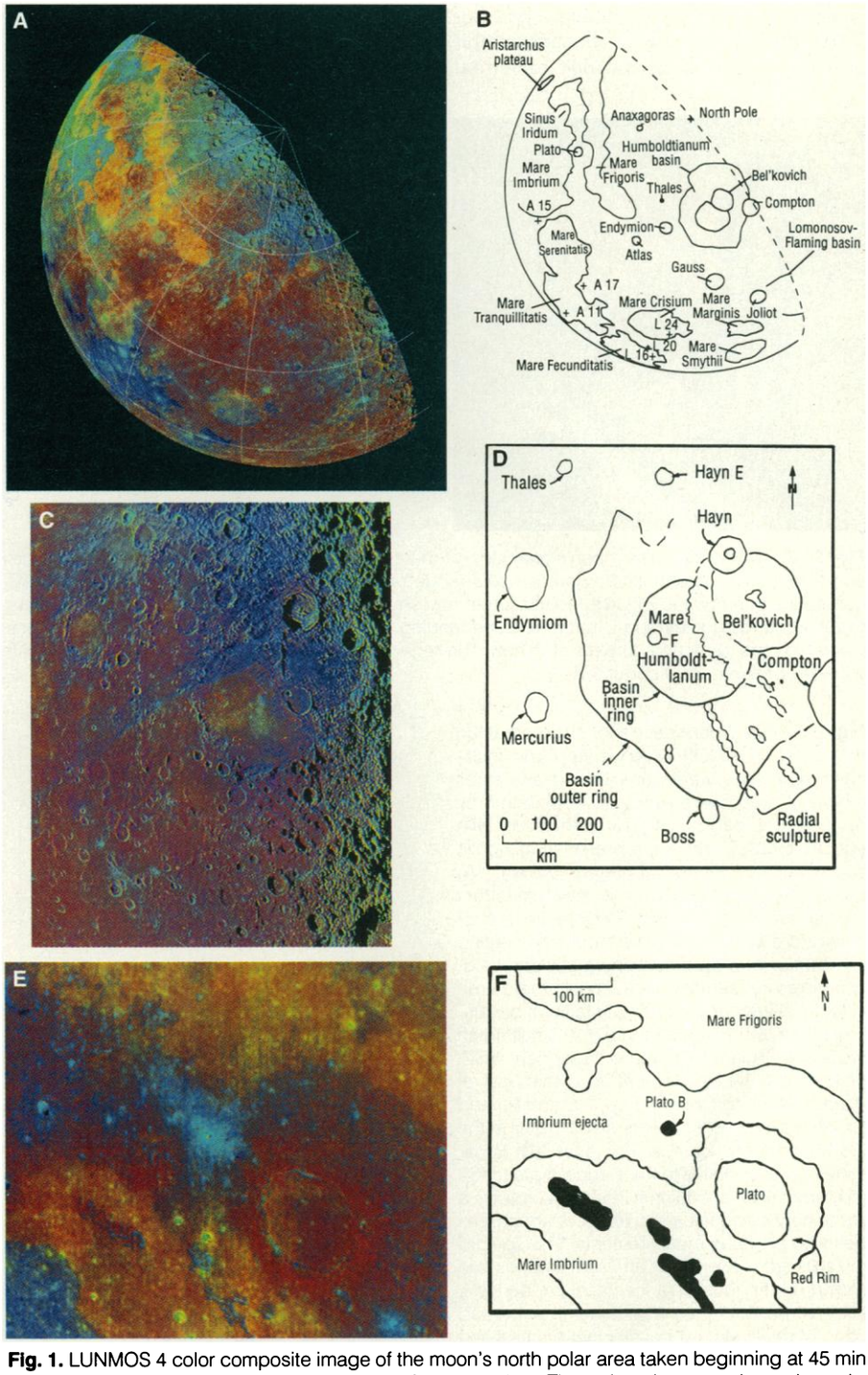

Fig. 1. LUNMOS 4 color composite image of the moon's north polar area taken beginning at 45 min before lunar closest approach at a range of 113,000 km. The solar phase angle at the subspacecraft point is 78°. Striations seen at the limit of resolution are artifacts resulting from data compression. (**A**) 756/413-, 756/986-, and 413/756-nm image ratios displayed as red, green, and blue, respectively. Red areas indicate primarily anorthositic highlands or impact melt rings; yellow-orange regions indicate iron-rich maria; blue regions in maria are generally more titanium-rich; light blue areas indicate Copernican soils (generally, fresh impact crater ejecta); and dark blue or purplish regions occur over dark mantle deposits. (**B**) Index sketch map corresponding to (A); A refers to Apollo landing sites and L refers to Luna landing sites. (**C**) The Humboldtianum basin prepared as in (A). Much of the blue material is related to ejecta from Hayn and other young craters. (**D**) Sketch map of Humboldtianum as shown in (C). The angularity of the outer ring is indicated as well as the radial texture between the inner and outer ring. (**E**) Plato crater as prepared in (A). (**F**) Sketch map of Plato crater as shown in (E), indicating the distinctive red rim surrounding the crater. Within Mare Imbrium, solid black represents Imbrium basin rings surrounded by subsequent mare deposits. Higher TiO_2 content plains in the upper left appear blue.

some of the late basalts filling Mare Imbrium (6). Fresh craters in all maria exhibit a strong 1-μm absorption due to ferrous iron, principally in pyroxene. Craters in the more titanium-rich basalts (such as Blue crater #1) are also brighter at 413 nm than their low titanium counterparts. On the eastern limb, mare units in craters Lomonosov and Maxwell have cratering model ages ranging from 3.73 to 3.81 Ga. The SSI data indicate that they are medium high titanium basalt soils with higher Ti content than inferred from Mariner 10 data (*23*). These basalts may be associated with the Lomonosov-Fleming basin, where dark-halo craters have been observed (*16*), suggesting the presence of cryptomaria. To the west, maria fill the craters Hubble and Joliot north of Mare Marginis. The Hubble mare is a medium high titanium basalt and has a cratering model age of 3.80 Ga, whereas the Joliot mare is a medium titanium basalt and has a cratering model age of 3.65 Ga. The SSI spectra indicate that Mare Smythii consists of medium titanium basalts but with a titanium content slightly higher than most mare units on the northeastern limb.

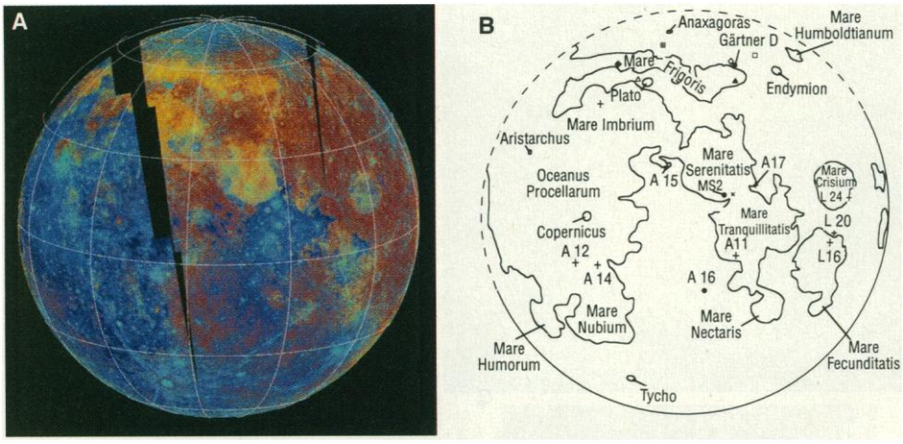

Fig. 2. (**A**) LUNMOS 7. The moon's near side prepared as in Fig. 1A and taken beginning 4 hours and 2 min after lunar closest approach at a range of 169,000 km. The solar phase angle at the sub-spacecraft point is 21°. (**B**) Index sketch map showing the principal named features; A refers to Apollo landing sites and L refers to Luna landing sites. The symbols correspond to locations where spectral data (Fig. 3) were obtained. The region without data was the result of a spacecraft software problem, now corrected.

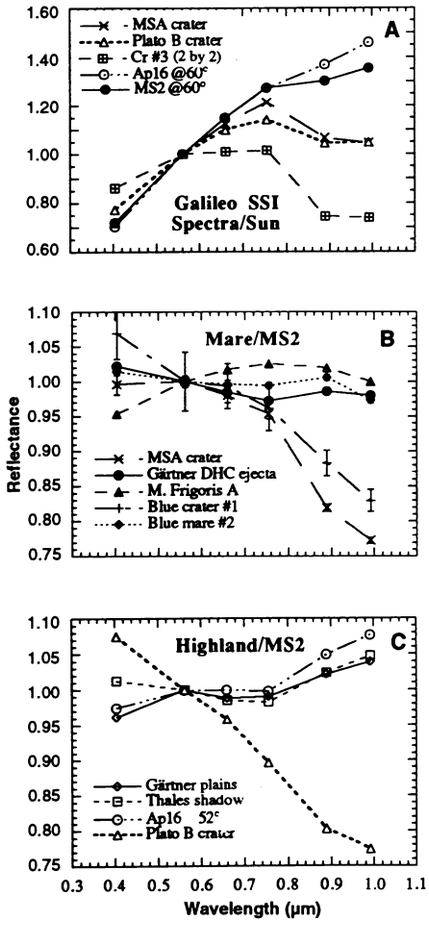

Fig. 3. SSI six-color spectra for small areas on the moon (LUNMOS 4 sequence). The multispectral images were coregistered and small blocks of pixels were averaged (2 by 2 to 5 by 5). Spectral calibration was performed with spectra for MS2 and of a representative Apollo soil measured in the laboratory (Ap16). (**A**) Lunar spectra relative to the solar spectrum (scaled to unity at 560 nm). Two spectra are for standard areas: Ap16 is the Apollo 16 landing site (a highland area containing low iron, feldspathic soils), and MS2 is a smooth mare area in Mare Serenitatis (medium-titanium basalt). The other three spectra are for small fresh craters: MSA is a fresh mare crater near MS2, Plato B is a feldspathic crater to the west of Plato on the Imbrium rim (Fig. 1, E and F), and Cr #3 is centered on a very small crater in the Fra Mauro formation near Epigenes. (**B**) Lunar mare spectra relative to the standard area MS2 (scaled to unity at 560 nm). The MSA crater is a secondary standard and this spectrum agrees well with previous measurements. The spectra for soils from two areas in Mare Frigoris are shown. M. Frigoris A (a low titanium, perhaps iron-rich basalt) is representative of the broad band of relatively red basalts that occur along the length of Mare Frigoris. Blue mare #2 (a medium to medium high titanium basalt) is representative of the smaller amount of bluer mare materials in western Frigoris. The ejecta of crater Gärtner D, located on younger light plains, exhibit spectral properties comparable to those of the bluer mare basalts, strongly suggesting the existence of subsurface mare basalts in Gärtner. (**C**) Lunar highland spectra relative to the standard area MS2 (scaled to unity at 560 nm). Data for highland area Apollo 16 (Ap-16) were obtained at a phase angle of ~52° with the use of Earth-based telescopes. Both the light plains within Gärtner and the ejecta shadow zone of Thales exhibit classic highland soil characteristics. The relative spectrum for Plato B, a typical feldspathic crater, is shown for comparison.

Dark mantle deposits (DMD) occur in association with some craters and as more extensive units (*27*), and are considered to be pyroclastic materials (*28, 29*). Data from the EM-2 encounter (Fig. 1, A and B, and Fig. 2, A and B) show that DMD in craters Gauss and Messala (a small crater west of Gauss) have low 413/560-nm ratios and low 756/986-nm ratios, similar to values reported for the spectrally "red" DMD on the Aristarchus plateau that were interpreted to be soils containing iron-bearing glasses (*27, 30*). In contrast, "blue" DMD in Atlas and Franklin as well as newly discovered deposit in crater Hahn have high 413/560-nm ratios and low 756/986-nm ratios, similar to values obtained for DMD found at the Apollo 17 site where the materials consist of ilmenite-rich black spheres of volcanic origin that have a high titanium content (*27–29*). Thus, pyroclastic activity may have been more frequent on the northeastern limb than previously known.

Most of the large, morphologically fresh craters seen in Figs. 1 and 2 appear to have reddish colored ejecta deposits on and near the crater rims, which probably represent impact melts. The Plato anomaly is more intense than most, but the radial extent

This preliminary analysis shows that most of the basalts are low to medium titanium content lavas, with only limited exposures of medium high titanium materials. Higher titanium content lavas are associated with the interiors of ancient basins, as found on the western limb (*21*). Moreover, as also found on the western limb (*23*), there appears to be only slight heterogeneity among the lavas. This condition is in contrast to that of mare units on the near side that display much more diversity in composition, possibly reflecting differences in magma evolution, source regions, or crustal thicknesses.

relative to the crater diameter is very typical. Melt production increases with impact energy, such that only large craters are expected to produce significant quantities of melt (*31*). This melt is deposited as thin veneers, flows, and ponds (*32*), so that melt sufficient to affect the spectral reflectivity is expected to remain near the surface only for relatively large and young craters, postdating widespread resurfacing from impact basins. Smrekar and Pieters (*33*) showed that reflectance spectra of the anomalously red crater rings of Tycho and Copernicus are consistent with the presence of iron-bearing glass. The melt is concentrated near the crater rim because it is produced from the deepest ejected target material. Therefore, we expect that all craters larger than about 25 km in diameter and postdating the formation of the Imbrium basin will have anomalously red near-rim colors. This generalization is observed in the EM-2 data for the near-side craters Copernicus, Zucchius, Pythagoras, Carpenter, Philolaus, Plato, Archimedes, Theophilus, Langrenus, Plinius, Geminus, Fabricus, and Hainzel, as well as for the far-side craters Ohm, Vavilov, and Hausen (*5*). In the case of Copernican age craters, the spectral effects of fresh soils partly counteract the reddish melt, but they are still redder (and darker) than melt-free soils of similar age and composition. The most recent of the large Copernican age craters, such as Tycho, Jackson, and Kepler, have relatively red and dark rings as compared to crater interiors and outer ejecta and rays.

The flybys of the moon by Galileo in 1990 and 1992 provided calibrated multispectral coverage of about 75% of the lunar surface in the 400- to 1000-nm spectral region. The images cover well-characterized regions of the near side, including standard areas for remote sensing and sample sites, that have enabled the calibration of Galileo data for extrapolation to areas on the northern, eastern, and western limbs and the far side that previously lacked quantitative multispectral coverage.

REFERENCES AND NOTES

1. M. J. S. Belton *et al.*, *Science* **255**, 570 (1992).
2. J. W. Head *et al.*, *J. Geophys. Res.* **98**, 17149 (1993).
3. C. M. Pieters *et al.*, *ibid.*, p. 17127.
4. R. Greeley *et al.*, *ibid.*, p. 17183.
5. A. S. McEwen *et al.*, *ibid.*, p. 17207.
6. T. B. McCord, M. P. Charette, T. V. Johnson, L. A. Lebofsky, C. M. Pieters, *ibid.* **77**, 1349 (1972).
7. C. Pieters, *Proc. Lunar Planet. Sci. Conf.* **9**, 2825 (1978).
8. The SSI filter set is described by M. J. S. Belton *et al.* [*Space Sci. Rev.* **60**, 413 (1992)] and its relation to lunar compositional studies is described in (*1*).
9. B. K. Lucchitta, *U.S. Geol. Surv. Misc. Invest. Ser. Map I-1062* (1978).
10. D. E. Wilhelms, *U.S. Geol. Surv. Prof. Paper 1348* (1987), p. 1.
11. W. K. Hartmann and G. P. Kuiper, *Lunar Planet. Lab. Comm.* **1** (no. 12), plate 12.51 (1962).
12. T. V. Johnson *et al.*, *Proc. Lunar Planet. Sci. Conf.* **8**, 1013 (1977).
13. K. A. Howard, D. E. Wilhelms, D. H. Scott, *Rev. Geophys. Space Phys.* **12**, 309 (1974).
14. D. E. Wilhelms and J. F. McCauley, *U.S. Geol. Surv. Misc. Invest. Ser. Map I-703* (1971); N. J. Trask and J. F. McCauley, *Earth Planet. Sci. Lett.* **14**, 201 (1972); W. R. Muehlberger *et al.*, in "Apollo 16 Preliminary Science Report," *NASA SP-315* (1972), p. 6-1; G. E. Ulrich *et al.*, *U.S. Geol. Surv. Prof. Paper 1048* (1981), p. 1; J. M. Boyce *et al.*, *Proc. Lunar Planet. Sci. Conf.* **5**, 11 (1974); V. R. Oberbeck *et al.*, *Moon* **12**, 19 (1975).
15. G. Neukum, *Moon* **17**, 383 (1977); Habilitationsschriff, Ludwig Maximilianis Universität, Münich (1983); G. Neukum *et al.*, *Moon* **12**, 201 (1975).
16. P. H. Schultz and P. D. Spudis, *Proc. Lunar Planet. Sci. Conf.* **10**, 2899 (1979).
17. J. W. Head and L. Wilson, *Geochim. Cosmochim. Acta* **56**, 2155 (1992).
18. B. R. Hawke and J. F. Bell, *Proc. Lunar Planet. Sci. Conf.* **12**, 665 (1981); J. F. Bell and B. R. Hawke, *J. Geophys. Res.* **89**, 6899 (1984).
19. B. R. Hawke *et al.*, *Lunar Planet. Inst. Tech. Report 92-09* (1992), p. 14.
20. J. W. Head *et al.*, *Lunar Planet. Sci. Conf.* **24**, 629 (1993).
21. D. A. Williams, thesis, Arizona State University (1992); S. D. Kadel, thesis, Arizona State University (1993).
22. M. P. Charette, T. B. McCord, C. M. Pieters, J. B. Adams, *J. Geophys. Res.* **79**, 1605 (1974); M. P. Charette, L. A. Sodenblom, J. B. Adams, M. J. Gaffey, T. B. McCord, *Proc. Lunar Planet. Sci. Conf.* **7**, 2579 (1976).
23. M. R. Robinson, B. R. Hawke, P. G. Lucey, G. A. Smith, *J. Geophys. Res.* **97**, 18 (1992).
24. D. E. Wilhelms and F. El Baz, *U.S. Geol. Surv. Misc. Invest. Ser. Map I-948* (1977).
25. J. W. Head *et al.*, in *Mare Crisium: A View from Luna 24*, R. B. Merrill and J. J. Papike, Eds. (Pergamon, New York, 1978), pp. 43–74.
26. B. L. Barsukov *et al.*, *Proc. Lunar Planet. Sci. Conf.* **8**, 3319 (1977).
27. L. R. Gaddis, C. M. Pieters, B. R. Hawke, *Icarus* **61**, 461 (1985).
28. L. Wilson and J. Head, *J. Geophys. Res.* **86**, 2971 (1981).
29. G. Heiken *et al.*, *Geochim. Cosmochim. Acta* **38**, 1703 (1974).
30. B. R. Hawke *et al.*, *Proc. Lunar Planet. Sci. Conf.* **21**, 377 (1991).
31. R. A. F. Grieve *et al.*, in *Impact and Explosion Cratering*, D. J. Roddy, R. O. Pepin, R. B. Merrill, Eds. (Pergamon, New York, 1977), pp. 791–814.
32. B. R. Hawke and J. W. Head, *ibid.*, p. 815.
33. S. Smrekar and C. M. Pieters, *Icarus* **63**, 442 (1985).

34. We thank the Galileo Project Office, the National Aeronautics and Space Administration (NASA), and numerous individuals who participated in the mission planning and initial data analysis, including C. Avis, T. Becker, L. Bolef, N. Bridges, C. Cunningham, E. DeJong, K. Edwards, E. Fischer, R. Garstang, A. Harch, S. Kadel, R. Kirk, J. Moersch, J. Plutchak, M. Robinson, R. Sullivan, W. Sullivan, J. Sunshine, S. Vail, L. Wainio, D. Williams, and J. Yoshimizu. The Galileo data set is available on CD-ROM through the NASA Planetary Data System. The National Optical Astronomy Observatories are operated by AURA, Inc., under a cooperative agreement with the National Science Foundation.

17 September 1993; accepted 24 March 1994

Rechargeable Lithium Batteries with Aqueous Electrolytes

Wu Li, J. R. Dahn,* D. S. Wainwright

Rechargeable lithium-ion batteries that use an aqueous electrolyte have been developed. Cells with $LiMn_2O_4$ and VO_2(B) as electrodes and 5 M $LiNO_3$ in water as the electrolyte provide a fundamentally safe and cost-effective technology that can compete with nickel-cadmium and lead-acid batteries on the basis of stored energy per unit of weight.

During the 1970s and 1980s, rechargeable lithium batteries were touted by some researchers as providing a possible long-term solution to the electric vehicle (EV) battery problem. The cells had about twice the energy density (measured by watt-hours stored per kilogram of battery) of the best competing ambient temperature batteries. Many companies moved to commercialize the technology, beginning with small cells for consumer applications, in view of the large markets anticipated. These cells used lithium metal as the negative electrode, a transition metal oxide [such as MnO_2 (*1*)] or chalcogenide [such as $NbSe_3$ (*2*)] as the positive electrode, and a nonaqueous electrolyte containing dissolved Li ions.

The operation of such cells is based on the ability of the positive electrode material to reversibly "intercalate" Li. Intercalation is the insertion of a guest atom (Li, for instance) into a host solid (such as MnO_2), accompanied by only slight, reversible structural changes in the host. Hosts for intercalation are commonly layered compounds such as graphite (*3*) or tunnel compounds such as MnO_2 or $LiMn_2O_4$ (*4*), in which the intercalated Li can reside between the layers or in the tunnels. Intercalation of Li occurs because the chemical potential of Li can be lowered when the Li atom is inserted into the host, thus forming chemical bonds.

The binding energy of Li when intercalated into a variety of hosts has been measured with respect to the binding energy of Li metal (Fig. 1). In each of the hosts listed,

W. Li and J. R. Dahn, Department of Physics, Simon Fraser University, Burnaby, British Columbia, Canada V5A 1S6.

D. S. Wainwright, Moli Energy (1990) Limited, 20000 Stewart Crescent, Maple Ridge, British Columbia, Canada V2X 9E7.

*To whom correspondence should be addressed.